Disjoining Pressure Effects in Ultra-Thin Liquid Films in Micropassages—Comparison of Thermodynamic Theory With Predictions of Molecular Dynamics Simulations

V. P. Carey
e-mail: vcarey@me.berkeley.edu

A. P. Wemhoff
e-mail: wemhoff2@llnl.gov

Mechanical Engineering Department,
University of California,
Berkeley, CA 94720-1740

The concept of disjoining pressure, developed from thermodynamic and hydrodynamic analysis, has been widely used as a means of modeling the liquid-solid molecular force interactions in an ultra-thin liquid film on a solid surface. In particular, this approach has been extensively used in models of thin film transport in passages in micro evaporators and micro heat pipes. In this investigation, hybrid μ*PT molecular dynamics (MD) simulations were used to predict the pressure field and film thermophysics for an argon film on a metal surface. The results of the simulations are compared with predictions of the classic thermodynamic disjoining pressure model and the Born-Green-Yvon (BGY) equation. The thermodynamic model provides only a prediction of the relation between vapor pressure and film thickness for a specified temperature. The MD simulations provide a detailed prediction of the density and pressure variation in the liquid film, as well as a prediction of the variation of the equilibrium vapor pressure variation with temperature and film thickness. Comparisons indicate that the predicted variations of vapor pressure with thickness for the three models are in close agreement. In addition, the density profile layering predicted by the MD simulations is in qualitative agreement with BGY results, however the exact density profile is dependent upon simulation parameters. Furthermore, the disjoining pressure effect predicted by MD simulations is strongly influenced by the allowable propagation time of injected molecules through the vapor region in the simulation domain. A modified thermodynamic model is developed that suggests that presence of a wall-affected layer tends to enhance the reduction of the equilibrium vapor pressure. However, the MD simulation results imply that presence of a wall layer has little effect on the vapor pressure. Implications of the MD simulation predictions for thin film transport in micro evaporators and heat pipes are also discussed.*
[DOI: 10.1115/1.2349504]

Keywords: thin film, wall effects, disjoining pressure, molecular dynamics, vapor pressure

Introduction

The concept of disjoining pressure has become a well-established formalism for treating the effect of wall-fluid force interaction in thin liquid films [1]. A typical situation of interest is shown in Fig. 1. This figure shows a cross section of a passage carrying a stratified flow of liquid and vapor flow. A deeper central portion of the passage (location A) carries most of the liquid while the lateral portions (location B) carry a thin liquid film flow with film thickness δ_f. Since most of the interface is flat and separates the deeper liquid flow from the vapor, at equilibrium we expect that

$$P_{ve} = P_{l0} \tag{1}$$

where P_{l0} is the liquid pressure at the interface in the absence of wall attractive forces and P_{ve} is the vapor pressure.

In the thin liquid film at location B, the pressure in the liquid film is altered by force interactions between liquid molecules and atoms or molecules in the solid. Although Israelachvili [1] provides the general disjoining pressure relation for a film of specified thickness, we derive the same relation here using the potential energy due to the forces that the solid wall molecules exert on each fluid molecule. To determine the resulting pressure variation in the film, we considered the system shown in Fig. 2. Fluid and metallic solid interactions are modeled with a Lennard-Jones interaction potential having the form

$$\phi_{fs}(r) = -\frac{C_{\phi,fs}}{r^6}\left(1 - \frac{D_m^6}{r^6}\right) \tag{2}$$

We further assume that a similar form, with different constants, models the long-range attraction between a pair of two fluid molecules.

$$\phi_{ff}(r) = -\frac{C_{\phi,ff}}{r^6}\left(1 - \frac{D_f^6}{r^6}\right) \tag{3}$$

In the liquid and solid phases of interest here, the interactions between pairs of molecules are treated as independent and addi-

---

Contributed by the Heat Transfer Division of ASME for publication in the JOURNAL OF HEAT TRANSFER. Manuscript received August 26, 2005; final manuscript received March 1, 2006. Review conducted by Raj M. Manglik. Paper presented at the 2005 ASME International Mechanical Engineering Congress (IMECE2005), November 5–11, 2005, Orlando, Florida, USA.

Copyright © 2006 by ASME

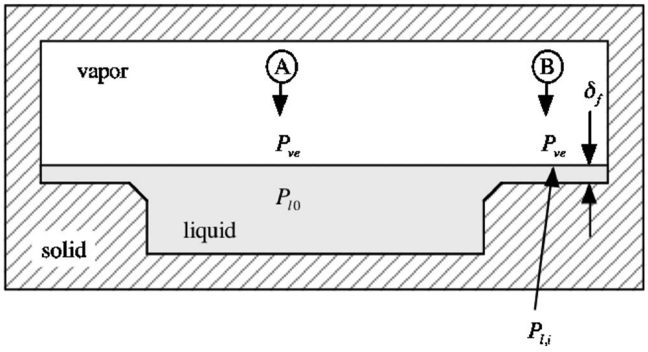

Fig. 1 Cross section of a micropassage containing thin liquid films

tive. D_m is the closest approach distance of fluid to solid molecules, and D_f is the closest approach distance of two fluid molecules. D_m and D_f are on the order of mean diameters for the molecular species involved. To get the total effect of all the solid metallic molecules on a given free fluid molecule, we integrate the product of the density and molecular potential to sum the contributions of all the solid molecules. It follows that the mean-field potential energy felt by the free fluid molecule due to interactions with all the metallic solid molecules is

$$\Phi_{fmf} = \int_{z_s=z}^{\infty} \int_{x=0}^{\infty} \rho_s \phi_{fs} (2\pi x)\, dx\, dz_s \tag{4}$$

Substituting the relation (2) above for the molecular potential, substituting x^2+z^2 for r^2, and integrating yields

$$\Phi_{fmf} = -\frac{\pi \rho_s C_{\phi,fs}}{6z^3} + \frac{\pi \rho_s C_{\phi,fs} D_m^6}{45 z^9} \tag{5}$$

For convenience, we reorganize the relation above in terms of a modified Hamaker constant A_{ls} defined as

$$A_{ls} = \pi^2 \rho_f \rho_s C_{\phi,fs} \tag{6}$$

Using these definitions converts Eq. (5) to the form

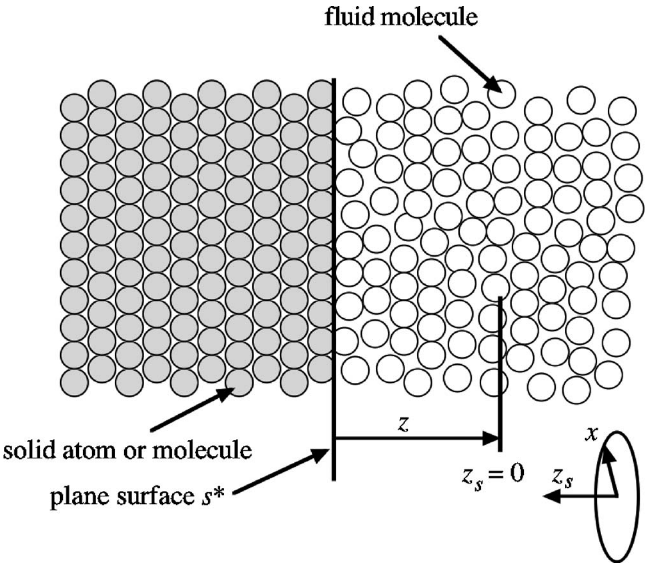

Fig. 2 Schematic used for derivation of disjoining pressure

$$\Phi_{fmf} = \frac{A_{ls}}{6\pi \rho_f D_m^3} \left[\frac{2}{15} \left(\frac{D_m}{z} \right)^9 - \left(\frac{D_m}{z} \right)^3 \right] \tag{7}$$

This potential is equivalent to a body force that produces a hydrostatic variation of pressure similar to that produced by gravity. We determine the pressure field by using the wall potential to determine the body force in the Navier-Stokes equations with no velocity terms,

$$0 = -\frac{1}{(\rho_f M/N_A)} \nabla P + \boldsymbol{f}_{fs} \tag{8}$$

In the above equation, $\boldsymbol{f}_{fs}$ is the force per unit mass on the fluid system. The force exerted on a single molecule by the entire wall is given by

$$\boldsymbol{F}_{fs} = -\nabla \Phi_{fmf} = \frac{A_{ls}}{2\pi \rho_f D_m^4} \left[\frac{2}{5} \left(\frac{D_m}{z} \right)^{10} - \left(\frac{D_m}{z} \right)^4 \right] \boldsymbol{z} \tag{9}$$

where $\boldsymbol{z}$ is the unit vector in the z direction, and the corresponding force per unit mass is

$$\boldsymbol{f}_{fs} = \frac{N_A \boldsymbol{F}_{fs}}{M} = \frac{N_A A_{ls}}{2\pi M \rho_f D_m^4} \left[\frac{2}{5} \left(\frac{D_m}{z} \right)^{10} - \left(\frac{D_m}{z} \right)^4 \right] \boldsymbol{z} \tag{10}$$

The force per unit mass specified by Eq. (10) is substituted into Eq. (8), and since the force only acts in the z direction, the relation simplifies to

$$\frac{dP}{dz} = \frac{A_{ls}}{2\pi D_m^4} \left[\frac{2}{5} \left(\frac{D_m}{z} \right)^{10} - \left(\frac{D_m}{z} \right)^4 \right] \tag{11}$$

Integrating both sides of Eq. (11) from a position z to ∞, and taking the pressure at ∞ to be P_{l0}, the resultant expression for the pressure profile close to the wall is

$$P(z) = P_{l0} - \frac{A_{ls}}{6\pi D_m^3} \left[\frac{2}{15} \left(\frac{D_m}{z} \right)^9 - \left(\frac{D_m}{z} \right)^3 \right] \tag{12}$$

Because D_m is on the order of a molecular diameter, and we are interested in z values larger than that, the z^{-9} term in Eq. (12) may be neglected. The relation for the pressure profile then simplifies to

$$P(z) = P_{l0} + \frac{A_{ls}}{6\pi z^3} \tag{13}$$

In the thin liquid film at location B in Fig. 1, we therefore expect the pressure to vary with distance from the lower wall according to Eq. (13). It follows that at the interface ($z = \delta_f$), the pressure in the liquid $P_{l,i}$ must be

$$P_{l,i} = P(\delta_f) = P_{l0} + \frac{A_{ls}}{6\pi \delta_f^3} \tag{14}$$

Combining Eqs. (1) and (14) and solving for $P_{ve} - P_{l,i}$ yields

$$P_{ve} - P_{l,i} = -\frac{A_{ls}}{6\pi \delta_f^3} \tag{15}$$

The amount by which P_{ve} differs from $P_{l,i}$ is the disjoining pressure P_d

$$P_d = -\frac{A_{ls}}{6\pi \delta_f^3} \tag{16}$$

Thus, for the circumstances depicted in Fig. 1, the pressure difference across the interface is equal to the disjoining pressure, which increases rapidly in magnitude as the film grows thinner. The result provided by Eq. (16) is also given in many texts (e.g., [1]).

The alteration of the equilibrium vapor pressure and liquid pressure in the film associated with disjoining pressure effects has been shown to alter the thermodynamic equilibrium conditions at the liquid-vapor interface of thin liquid films. The resulting shift in the vapor-pressure versus temperature relation must be taken into account when modeling thin film evaporation or condensation processes in micropassages of micro heat pipes and micro capillary-pumped loops. Consequently, the effects of disjoining pressure have been explored in a variety of circumstances typically encountered in these types of applications [2–13]. While the concept of disjoining pressure provides a framework for analyzing the effects of wall-fluid attractive forces, it ignores many of the detailed features of the liquid film. In the work summarized here, molecular dynamics simulations were used to explore the detailed features of the structure and thermophysics of thin liquid films on a solid surface. The predicted film features and equilibrium vapor pressure were examined for films of varying thickness and the results were compared to predictions of the conventional disjoining pressure treatment. These comparisons are described in the following sections of this paper.

MD Simulation of Thin Liquid Films

As a means of assessing the validity of the pressure profile predicted by our thermodynamic model, we also modeled the molecular level behavior of liquid argon near a solid gold (metallic) wall using a classical molecular dynamics (MD) simulation. The hybrid molecular dynamics simulation technique used here combines traditional *NVE*-type MD simulation techniques with a stochastic boundary condition used for the equilibration of pressure. Several aspects of the methodology presented here have been previously described [14]. However, some adjustments have been made in this study to obtain as accurate a value of saturation pressure as possible. This methodology allows for the implementation of monatomic fluids that interact via the well-known Lennard-Jones 6-12 potential,

$$\phi_{LJ}(r) = 4\varepsilon_{LJ}\left[\left(\frac{\sigma_{LJ}}{r}\right)^{12} - \left(\frac{\sigma_{LJ}}{r}\right)^{6}\right] \tag{17}$$

where σ_{LJ} and ε_{LJ} are the Lennard-Jones length and energy parameters, respectively, and r is the distance between two molecules. For this methodology, the particles are initialized in either a face-centered-cubic (fcc) lattice or in a cubic lattice whose densities matched the values for bulk phases at the desired equilibrium temperature (the cubic lattice is used in lieu of the standard fcc lattice for placement of individual layers of molecules for modeling ultra-thin films). The molecules are also initialized with velocities matching the Boltzmann distribution for a low initial temperature ($T_r = T/T_c = 0.1$) using the Box-Mueller algorithm [15]. The system equilibrates by raising the system temperature from the initially low value to the desired equilibrium temperature via velocity rescaling such that the system kinetic energy adheres to the relation

$$\frac{1}{2}m\sum_{i=1}^{N} c_i^2 = \frac{3}{2}Nk_BT \tag{18}$$

This rescaling is executed for 30,000 steps, and then the system was allowed to equilibrate with the rescaling turned off for an additional 20,000 steps. Upon equilibration, the simulation domain is evenly divided into 100 bins along the z axis for collection of mean density values during subsequent time steps.

The hybrid MD simulation domain utilized in this study, depicted in Fig. 3, features three types of boundaries: periodic, wall, and flux. Periodic boundaries exist at all four boundaries in the x and y directions. The $z = 0$ boundary represents the solid surface and features a wall potential, Φ_{fmf}, which binds the liquid film to a semi-infinite metal solid. The wall potential (7) was used here with the constant values

$$A_{ls} = 1.01 \times 10^{-19}\ \text{J} \tag{19a}$$

$$D_m = 0.304\ \text{nm} \tag{19b}$$

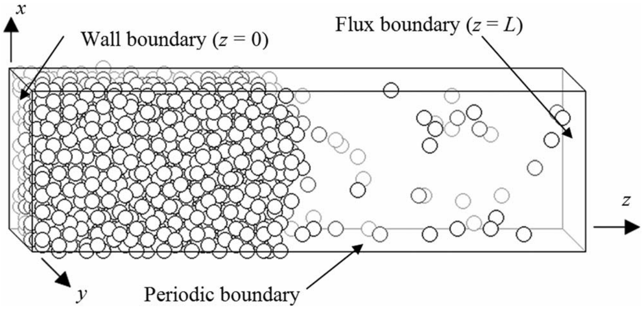

Fig. 3 MD simulation domain

$$\rho_f = 2.08 \times 10^{28}\ \text{m}^{-3} \tag{19c}$$

which are appropriate for argon on a metal surface. Note that this 9-3 version of the wall potential (7) is slightly different than the 10-4 model given by Toxvaerd [16] for an fcc Lennard-Jones solid lattice. However, a 9-3 potential has been previously used in some studies of Lennard-Jones molecules interacting with a surface (e.g., [17,18]).

A flux boundary at $z = L$ is used to adjust the system pressure to an equilibrium value. For an ideal gas, the flux J (in molecules/m^{2}s) is related to the system pressure P and temperature T by the kinetic theory relation [19]

$$J = \sqrt{\frac{k_BT}{2\pi m}}\left(\frac{P}{k_BT}\right) \tag{20}$$

where m is the molecular mass of the injected species. Note that the flux boundary borders on the vapor region of the simulation domain as shown in Fig. 3, allowing for the ideal gas approximation in the derivation of Eq. (20). The concept behind the flux condition is similar to that provided by an Andersen thermostat [20], where system molecules randomly collide with a fictitious surrounding infinite heat bath to maintain a constant system temperature. In the hybrid simulation, the flux boundary separates the simulation domain from an infinite vapor bath, and the flux supplied by Eq. (20) represents an equilibrium value for the vapor bath of specified temperature and pressure. Frenkel and Smit discuss this concept further for a Monte Carlo simulation [21]. The treatment of the vapor as an ideal gas is not completely accurate for a vapor at saturation. However, we adopt this idealization here since it is a good approximation at low vapor densities, and it is consistent with idealizations made in formulation of conventional disjoining pressure, as discussed in the next section.

The flux boundary acts to inject a molecule stochastically into the simulation domain at a desired interval. During the initial 50,000 steps of the simulation, the boundary acts to preserve mass, hence when a molecule leaves the $z = L$ boundary, another molecule is injected directly into the simulation domain through that same boundary. After the kinetic energy equilibration period, molecules are injected corresponding to a desired pressure using Eq. (20). When a molecule is injected, the position of the molecule is chosen randomly on the flux boundary plane. The x and y velocities adhere to the Boltzmann distribution for a bulk gas, while the z velocity is sampled from the distribution [22]

$$f(v_z)dv_z = \frac{mv_z}{k_BT}e^{-mv_z^2/2k_BT}dv_z \tag{21}$$

where $f(v_z)$ represents the fraction of molecules of a large sample with z-velocity components between v_z and $v_z + dv_z$. Sampling of the x- and y-velocity distributions is performed via the Box-Mueller algorithm [15], while the z velocity is sampled using the relation

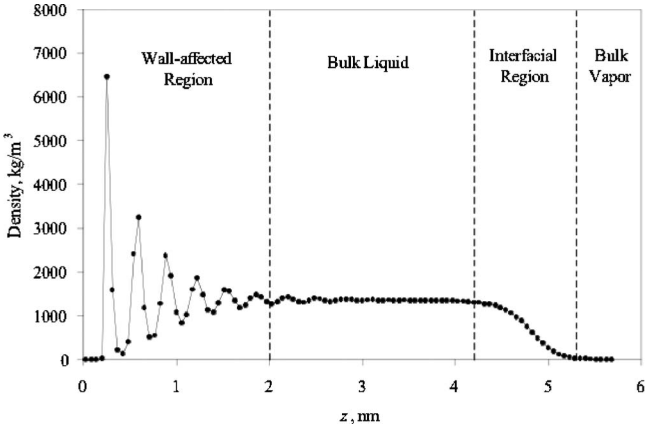

Fig. 4 Argon liquid film mass density profile: $T_r=0.57$, 100 collection bins, and 400,000 time steps

$$v_{z,i} = -\sqrt{-\log(\Re)\left(\frac{2k_BT}{m}\right)} \tag{22}$$

where $\Re$ is a random number between 0 and 1.

The system is equilibrated by adjusting the input flux every 50,000 time steps to force the loss of molecules from the simulation domain to match the gain from the flux boundary. The adjustment is performed by determining the net outflux of molecules per time step over the 50,000-step period by applying a fit curve to the system molecule count variation with time. Unlike previous work [14], however, the injected flux value was adjusted via the equation

$$J_{\text{new}} = \frac{1}{2}(J_{\text{old}} - J_{\text{slope}}) \tag{23}$$

where J_{new} is the updated flux, J_{old} is the previous flux, and J_{slope} is the average net influx of molecules over the previous 50,000 steps determined using the fit curve, and the factor of one-half was used to prevent overshoot.

For this study, a simulation of argon molecules was used, where values of σ_{LJ} and ε_{LJ} were taken to be 0.34 nm and 1.67×10^{-21} J ($\varepsilon_{LJ}/k_B=121$ K), respectively. Both the forces and intermolecular potentials were smoothly truncated at the cutoff radius of $5.0\sigma_{LJ}$ using standard truncation algorithms for short-ranged forces [23]. The time step used in the simulations was 5 fs, and the configuration was updated at each step by the velocity Verlet algorithm [23]. The initial liquid film lattice consisted of $c_Z \times 6 \times 6$ primitive fcc cells, where c_Z is the number of cells in the z direction. The initial vapor lattice size depended on the system temperature.

A typical average mass density profile through the simulation domain is shown in Fig. 4. The attraction of the wall potential causes an ordering of molecules in the wall-affected region of the liquid that results in peaks in the density profile. These peaks rapidly diminish where the wall potential becomes repulsive ($z < (2/5)^{1/6} D_m$). A similar wall-region profile for argon was exhibited in the MD simulation of Liu [24], and in the application of the Born-Green-Yvon equation for argon on graphite [18] and for binary Lennard-Jones fluids on a surface [25], although these comparisons are qualitative and are strongly dependent upon the parameters used in the wall potential [18]. At a value of approximately 2.0 nm from the wall, the density profile becomes approximately uniform, suggesting the transition to a bulk liquid region. At 4.2 nm from the wall the rapid decrease in the density profile suggests an interfacial region, while beyond 5.3 nm the uniform low density profile indicates a bulk vapor region. Values of the bulk liquid density as a function of temperature compared well with ASHRAE recommended values [26].

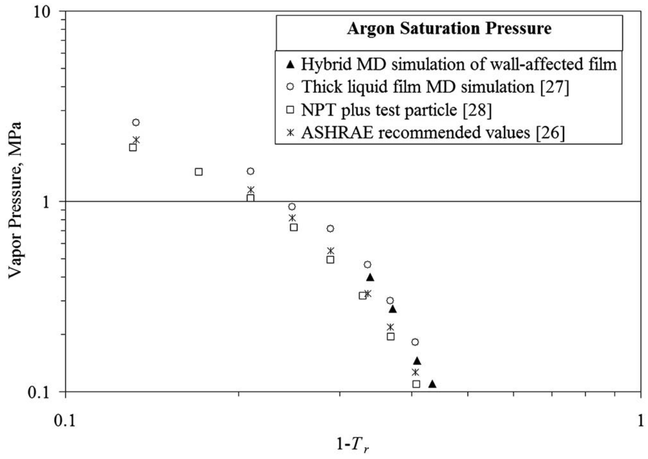

Fig. 5 Simulated argon vapor pressure values from the hybrid MD simulation of the wall-affected film compared to results for a simulated thick liquid film, the NPT plus test particle method, and ASHRAE recommended values. Simulations were run for 400,000 time steps for this study.

Once the equilibrium flux at the $z=L$ boundary was found, the value of pressure was determined from Eq. (20). Figure 5 shows the mean pressure values derived from the hybrid MD method for a thick argon film ($\delta_f > 15$ nm) compared to values given by ASHRAE tables [26] as a function of the departure from the critical point, 1-T_r. Also shown in Fig. 5 are the thick film values from argon simulations by Dunikov et al. [27] for a cutoff of $3.5\sigma_{LJ}$ and values taken from vapor phase equilibria MD simulations by Lotfi et al. using the NPT plus test particle method [28]; the cited data were adjusted using the values of σ_{LJ} and ε_{LJ} for this study. The figure depicts that, for thick films, the predicted vapor pressure variation for our hybrid model is comparable to the ASHRAE data and results of other MD simulations, regardless of the inhomogeneity of the fluid.

For any equilibrium saturation pressure value shown in Fig. 5, the resultant local pressure profile can be determined from MD simulations using the modified virial calculation by Weng et al. [29] and by fixing the external pressure to the specified value. One example of this is shown in Fig. 6 for $T_r=0.6$, where the pressure

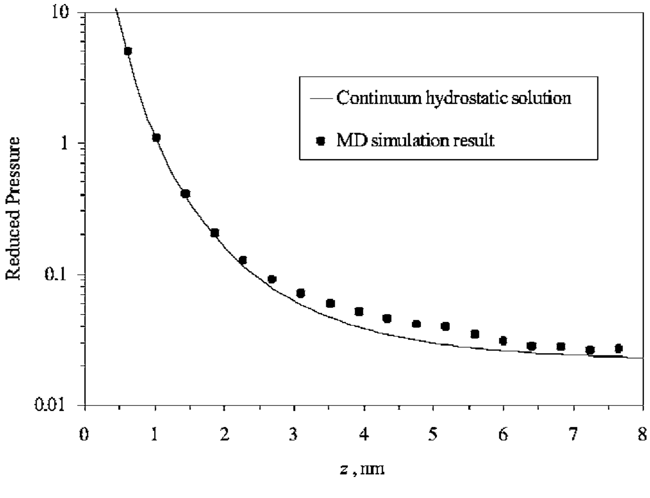

Fig. 6 Calculated local pressure profile for argon on a metallic solid surface using MD and hydrostatic analyses; external conditions match saturation data for argon at 1 atm. Simulation featured 300,000 time steps, 50 collection bins, and approximately 1980 molecules.

profile in the film was also predicted by the hydrostatic model in Eq. (12) using A_{ls} and D_m values similar to those in Eqs. (19*a*) and (19*b*).

It should be noted that equilibrium mean local pressure values extracted from the simulation domain far from the wall compared well with the applied external vapor pressure values for the simulations in this study. Therefore, the flux boundary method provides a viable alternative to traditional domain volume rescaling methods for system pressure management. Furthermore, since the hybrid method allows for system readjustment towards equilibrium (as described above), then the equilibrium system by definition would have a constant chemical potential in both phases, and thus a grand canonical system (μPT) is simulated.

Theoretical analyses of thin films on solid surfaces suggest that the saturation pressure decreases with thickness for very thin films [30]. The results described above indicate that the hybrid MD simulation scheme predicts the equilibrium vapor pressure with reasonable accuracy for thick films. It is therefore plausible to expect that it will provide physically realistic predictions of how the vapor pressure varies with film thickness. Exploration of the effects of film thickness on equilibrium vapor pressure is described in the following sections.

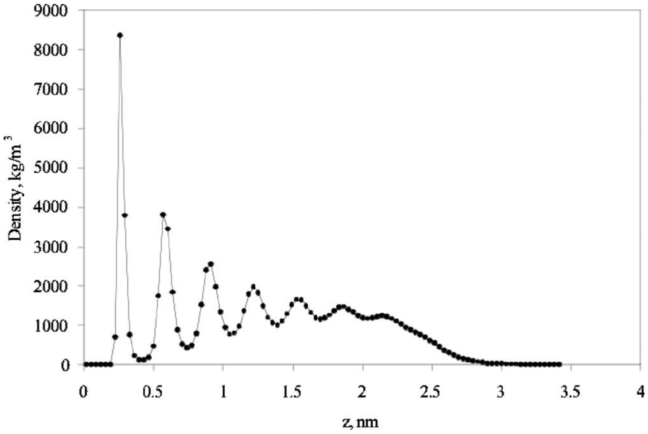

Fig. 7 Mass density profile for argon film on solid surface, T_r =0.6. Film thickness was calculated as 2.6 nm. Simulation was run with lateral dimensions of $10.0\sigma_{LJ}\times 10.0\sigma_{LJ}$ and 500,000 time steps.

Comparison to Disjoining Pressure Theory

Variation of the liquid film thickness produces disjoining pressure effects that alter the equilibrium vapor pressure from the normal bulk-fluid equilibrium value in standard saturation tables. The conventional thermodynamic analysis of these effects begins by integrating the Gibbs-Duhem equation

$$d\hat{\mu} = -\hat{s}dT + \hat{v}dP \tag{24}$$

at constant temperature from saturation conditions to an arbitrary state in the liquid and vapor phases. In doing so, we follow the usual conventions of treating the liquid as incompressible and the vapor as an ideal gas. This yields the following relations for the vapor and liquid chemical potentials in the absence of wall attraction effects:

$$\hat{\mu}_v = \hat{\mu}_{v,sat} + \bar{R}T \ln (P_{ve}/P_{sat}) \tag{25}$$

$$\hat{\mu}_l = \hat{\mu}_{l,sat} + \hat{v}_l(P_l - P_{sat}) \tag{26}$$

For a pure fluid, the chemical potential is equivalent to the specific Gibbs function

$$\hat{\mu}_l = \hat{g}_l$$

In the presence of wall attraction effects in the liquid film, the Gibbs function is augmented by the potential energy associated with interaction between fluid molecules and surface molecules or atoms. Denoting the potential energy per fluid molecule due to interaction with the wall as a whole as Φ_{fmf}, the expression for the liquid chemical potential becomes

$$\hat{\mu}_l = \hat{\mu}_{l,sat} + \hat{v}_l(P_l - P_{sat}) + N_A\Phi_{fmf} \tag{27}$$

For the system to be in equilibrium at the interface, the liquid pressure must equal the equilibrium vapor pressure

$$P_{l,i} = P_{ve} \tag{28}$$

and the chemical potentials must be equal there. Equating the right sides of Eqs. (25) and (27), and setting P_l equal to P_{ve} as dictated by Eq. (28), yields

$$\bar{R}T \ln (P_{ve}/P_{sat}) = \hat{v}_l(P_{ve} - P_{sat}) + N_A\Phi_{fmf} \tag{29}$$

which can be rearranged to the form

$$\frac{P_{ve}}{P_{sat}} = \exp\left\{\frac{P_{sat}\hat{v}_l}{\bar{R}T}\left(\frac{P_{ve}}{P_{sat}} - 1\right) + \frac{N_A\Phi_{fmf}}{\bar{R}T}\right\} \tag{30}$$

For the circumstances of interest here, P_{ve} is close to P_{sat} and $P_{sat}\hat{v}_l/\bar{R}T$ is small, with the net result that the first term in the curly brackets above is negligible compared to the second. Neglecting the first term simplifies Eq. (30) to the form

$$\frac{P_{ve}}{P_{sat}} = \exp\left\{\frac{\Phi_{fmf}}{k_BT}\right\} \tag{31}$$

Substituting the relation (7) derived previously for the wall potential, neglecting the z^{-9} term, and setting z equal to δ_f at the interface, the following relation is obtained

$$\frac{P_{ve}}{P_{sat}} = \exp\left\{-\frac{A_{ls}}{6\pi\rho_f\delta_f^3k_BT}\right\} \tag{32}$$

A key objective of this investigation was to determine if the MD simulation model predictions agreed with the variation of saturation pressure with film thickness indicated by Eq. (32).

To explore the predicted effect of film thickness on equilibrium saturation pressure, MD simulations of argon were performed at T_r=0.6 for films of various thicknesses. The parameters for the simulations were set at the values described in the previous section. In these runs, the initial thickness of the film was specified via the number of fcc cells in the z direction, and the initial thickness of the vapor region was kept constant at 2.0 fcc lattice parameters. It should be noted that the size of the vapor region has a significant effect on the calculated saturation pressure values due to the time required for molecular propagation across the vapor region during the 50,000-step sampling period. The thickness of the equilibrated film was calculated as the distance from the wall (z=0) to the center of the interfacial region, corresponding to

$$\rho = \rho_{m,\infty} = \frac{1}{2}(\rho_{l,\infty} + \rho_{v,\infty})$$

where $\rho_{l,\infty}$ and $\rho_{v,\infty}$ are the values of liquid and vapor bulk densities for films thick enough that disjoining effects are not present. The runs were performed for 500,000 time steps, over a range of film thickness from 0.7 to 4.9 nm. Figure 7 is a plot of the density profile for a thickness value of 2.6 nm, where one can observe that for this thickness value, very little bulk liquid density region is present. For T_r=0.6, the density transition associated with the interfacial region occupies a thickness of approximately 0.7 nm, and the wall-affected region has a thickness of about 2 nm, so the size

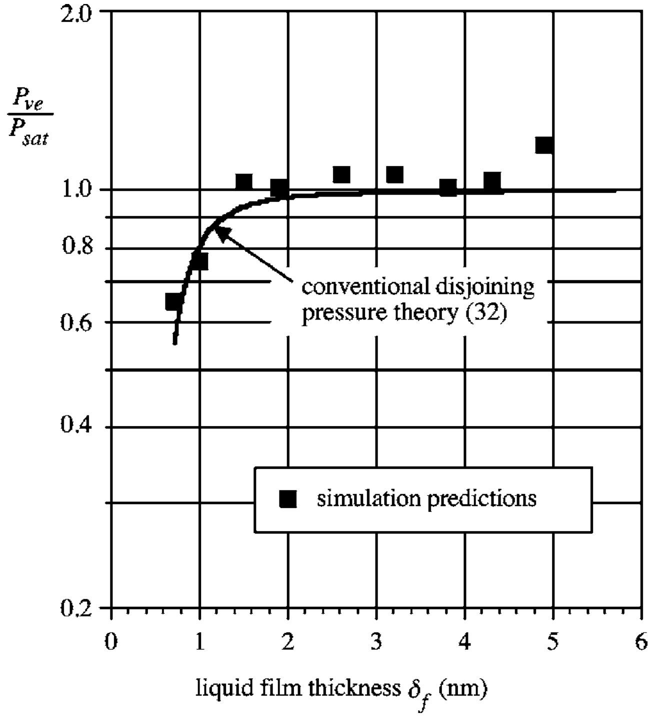

Fig. 8 Comparison of MD results with conventional theory

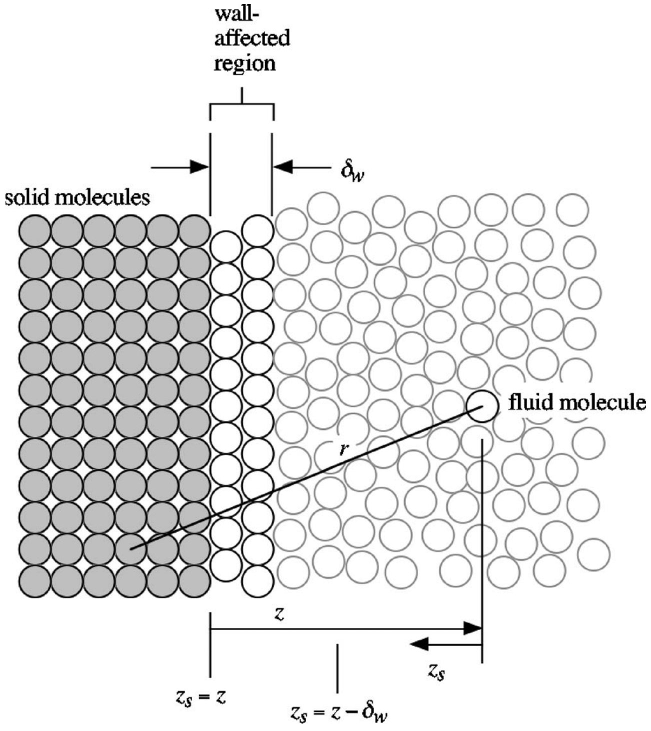

Fig. 9 Wall layer model

of the bulk liquid region tends to zero as the film thickness falls below 2.7 nm.

For films with thicknesses above 1.5 nm, the predicted vapor pressure agrees fairly well with the corresponding ASHRAE value [26]. Figure 8 presents the variation of P_{ve}/P_{sat} with film thickness predicted by our hybrid MD simulations for film thicknesses below 6 nm. In these results, the average of the final six calculated pressure values (step 250,000 through step 500,000) were used as data points. Also shown is the variation predicted by the theoretical relation (32) derived from conventional disjoining pressure theory. It can be seen in Fig. 8 that the MD simulation predictions generally agree with the tabulated bulk saturation pressure within about 10% at film thicknesses greater than 1.5 nm, with the exception of the film with thickness of 4.9 nm. Below 1.5 nm, the simulation vapor pressure predictions drop well below the equilibrium saturation pressure for the bulk phases at $T_r=0.6$. As indicated in Fig. 8, overall, the variation of equilibrium vapor pressure agrees well with the variation predicted by the conventional disjoining pressure theory.

As noted above, we found that the simulation predictions of equilibrium pressure were sensitive to vapor region thickness. Our initial simulation efforts were found to predict a vapor pressure variation with film thickness that differed significantly from conventional theory. We subsequently found that the periods between external flux adjustments were not long enough to fully equilibrate molecular exchange at the interface with the imposed flux boundary condition at the outer boundary of the simulation. The MD simulation results in Fig. 8 were obtained from simulation runs in which the simulation was run long enough that molecular exchange at the interface is in equilibrium with the outer boundary flux condition for the specified vapor region thickness.

While the agreement of the simulation predictions with conventional theory is reassuring, it is interesting that the MD simulations that include the effect of the wall-affected region produce a prediction that agrees so well with a thermodynamic theory that largely ignores such effects. The next section explores this issue further.

A Wall Layer Model

The peaks in the local mean density indicated in Figs. 4 and 7 reflect a layered order in the fluid molecules near the surface. The decreasing magnitude of the peaks with increasing distance from the solid wall indicates that the degree of organization in the layered structure of the fluid diminishes with distance from the wall. In a recent study of this type of liquid layering near a liquid-solid interface, Xue et al. [31] quantified this in terms of a planar structure factor that varied from 1 for a perfect fcc plane of molecules to 0 for molecules in random positions. The planar structure factor varies from close to 1 at the solid-liquid interface to close to 0 at larger distances from the wall. Xue et al. [31] found that for a wetting fluid, the planar structure factor decreased to 0 about two fluid molecular diameters away from the wall.

To explore how the liquid layering near the solid wall affects the disjoining pressure, a model is adopted here in which the fluid within two molecular diameters of the wall is treated as a solid phase of planar layers, and the fluid beyond two molecular diameters is treated as bulk fluid. This is obviously a crude approximation to the gradually diminishing layered structure in the fluid near the surface, but it captures the main features of the layering, and it is consistent with the results of Xue et al. [31] in that it limits the strongest layering effects to the region within two molecular diameters of the wall.

To develop this model with wall effects included, we consider the system shown in Fig. 9 in which fluid molecules interact with a composite wall structure. The composite wall is a semi-infinite region of solid metal wall molecules or atoms covered with a layer of fluid molecules that are modeled as being in a solid phase. The layer of fluid molecules has thickness δ_w. Because they are more localized in their position than molecules in the bulk liquid, molecules in the wall-affected region behave almost like a solid layer attached to the metal surface. The wall layer model proposed here is based on the reasoning that the presence of this layer causes molecules in the bulk liquid to behave as though they are interacting with a composite wall structure consisting of the metal substrate plus the strongly wall-affected layer. The molecules in the bulk fluid layer are presumed to behave as predicted by the bulk-fluid analysis in the previous section except that they are closer to the effective solid-liquid interface than would be the case if the wall-affected region were not considered to be part of the composite solid in Fig. 9. Although this model is simplistic, it accomplishes the objective of predicting the effect of the quasi-solid wall-affected layer on the force interaction potential Φ_{fmf} at the interface, which affects the vapor pressure as predicted by Eq. (31).

In this model, consistent with the reasoning above, we take δ_w to be two molecular diameters D_m. As in the first section of this paper, the fluid and metallic solid interactions and the interactions between fluid molecules are modeled with Lennard-Jones potentials (2) and (3). The interactions between pairs of molecules are treated as independent and additive. To get the total effect of all the solid metallic molecules and the solid layer molecules on a given free fluid molecule, we integrate the product of the density and molecular potential to sum the contributions of all the solid and layer molecules.

It follows that the mean-field potential energy felt by the free fluid molecule due to interactions with all the metallic solid molecules and the solid layer molecules is

$$\Phi_{fmf} = \int_{z_s=z-\delta_w}^{z_s=z} \int_{x=0}^{\infty} \rho_f \phi_{ff}(2\pi x)\, dx\, dz_s + \int_{z_s=z}^{\infty} \int_{x=0}^{\infty} \rho_s \phi_{fs}(2\pi x)\, dx\, dz_s \tag{33}$$

Substituting the relations (2) and (3) above for the molecular potentials, substituting x^2+z^2 for r^2, and integrating yields

$$\Phi_{fmf} = \frac{\pi\rho_f C_{\phi,ff}}{6}\left(\frac{1}{z^3} - \frac{1}{(z-\delta_w)^3}\right) - \frac{\pi\rho_f C_{\phi,ff} D_f^6}{45}\left(\frac{1}{z^9} - \frac{1}{(z-\delta_w)^9}\right) - \frac{\pi\rho_s C_{\phi,fs}}{6z^3} + \frac{\pi\rho_s C_{\phi,fs} D_m^6}{45z^9} \tag{34}$$

For $z > D_f$ or D_m, terms involving D_f and D_m are small and can be neglected. The potential is then well approximated as

$$\Phi_{fmf} = \frac{\pi\rho_f C_{\phi,ff}}{6}\left(\frac{1}{z^3} - \frac{1}{(z-\delta_w)^3}\right) - \frac{\pi\rho_f C_{\phi,fs}}{6z^3} \tag{35}$$

For convenience, we reorganize the relation above in terms of modified Hamaker constants A_{ls} defined by Eq. (6) and A_{ll} defined as

$$A_{ll} = \pi^2 \rho_f^2 C_{\phi,ff} \tag{36}$$

Using these definitions converts Eq. (35) to the form

$$\Phi_{fmf} = -\frac{A_{ls}}{6\pi\rho_f (z-\delta_w)^3}\left[\frac{(z-\delta_w)^3}{z^3}\left(1 - \frac{A_{ll}}{A_{ls}}\right) + \frac{A_{ll}}{A_{ls}}\right] \tag{37}$$

In this model, Eq. (31) from the thermodynamic analysis above still applies, with Φ_{fmf} evaluated at the interface z location, which is $z=\delta_f$. Using (37) to evaluate Φ_{fmf} with $z=\delta_f$, and neglecting $P_{sat}\hat{v}_l/\bar{R}T$ compared to terms of order one, we convert Eq. (31) to

$$\frac{P_{ve}}{P_{sat}} = \exp\left\{-\frac{A_{ls}}{6\pi(N_A/\hat{v}_l)(\delta_f-\delta_w)^3 k_B T}\left[\frac{(\delta_f-\delta_w)^3}{\delta_f^3}\left(1 - \frac{A_{ll}}{A_{ls}}\right) + \frac{A_{ll}}{A_{ls}}\right]\right\} \tag{38}$$

Figure 10 compares the MD simulation values of P_{ve}/P_{sat} with the profiles predicted using the conventional disjoining pressure theory (32) and the wall layer model (38). For our analysis, A_{ll} for argon was taken to be 2.57×10^{-20} J. This value was obtained using the relation for A_{ll} recommended by Israelachvili [1] with the value of surface tension for argon recommended by Ref. [26] at $T_r=0.6$.

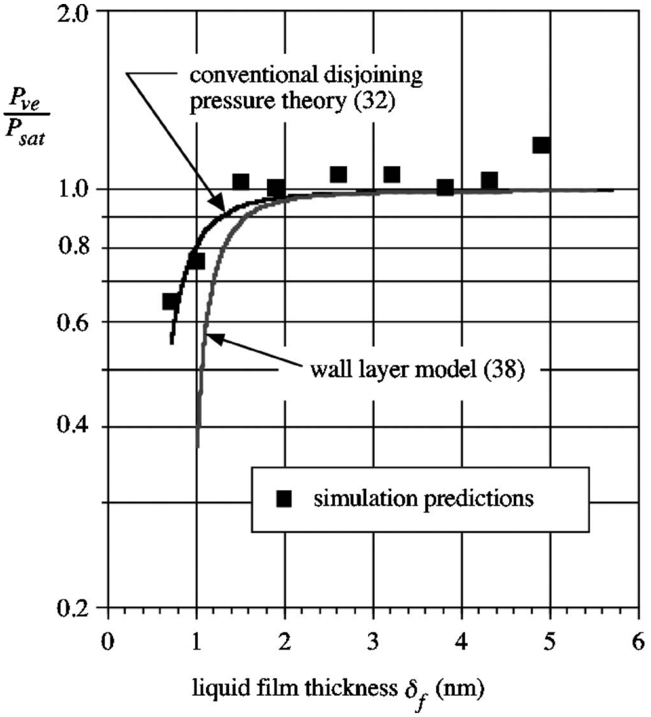

Fig. 10 Comparison of MD simulation results with predictions of conventional theory and the wall layer model

In this model, we have taken the density in the wall-affected region to be equal to the bulk liquid density. Because of the layered structure, the density may actually be slightly different in the wall-affected region. The density in this region would affect the A_{ll} value, as dictated by Eq. (36). Sensitivity calculations using Eq. (38) indicate that a 10% change in density in the wall-affected region would produce about a 20% change in A_{ll}, but only about an 8% change in P_{ve}/P_{sat}. Thus, taking the wall region density to equal the bulk density may produce some inaccuracy, but the effect on the vapor pressure prediction is estimated to be on the order of about 8%.

In comparing the different model predictions in Fig. 10, it should be noted that the MD simulation points for $\delta_f \leq 1.5$ nm correspond to a film with no bulk fluid region. Since the conventional theory applies to bulk fluid interacting with a wall, there is reason to expect that the vapor pressure predicted by the MD simulation may not agree with the conventional model prediction for these points. The MD simulation is expected to be a better prediction for such cases. As noted in the previous section, the conventional theory actually agrees well with the MD simulation predictions, even for $\delta_f \leq 1.5$ nm, where no conventional bulk liquid region exists in the film.

Figure 10 indicates that, relative to the predictions of the MD simulations, the wall layer model predicts a more rapid decrease of vapor pressure with decreasing film thickness. Hence, the wall layer model, which was expected to better model the impact of liquid layering near the wall, actually does not agree as well with the simulation predictions as the conventional theory. The wall layer model developed here assumes the extreme case in which the layers of fluid molecules closest to the wall behave as a solid, strongly resisting the forces of molecules farther from the surface. Even for this extreme case, the effect on vapor pressure is small, as indicated in Fig. 10. Our results suggest that when the fluid molecules in the layers near the wall are allowed some limited motion, as is the case in the MD simulations, the effect of their limited capability to move may have little influence on their force interaction with molecules further from the wall. The liquid film may then behave essentially as if the film were all bulk liquid with no layering near the wall. Overall, the results of our models and these observations suggest that liquid layering near the wall does not strongly influence the impact of wall attractive forces on the equilibrium vapor pressure in thin liquid films on solid surfaces.

Concluding Remarks

The hybrid MD simulations used in this investigation of thin liquid films predict vapor pressure values for thick films that agree well with tabulated values for saturated liquids. This agreement suggests that the predictions of this type of simulation for very thin films should be physically realistic. This lends some credibility to MD simulation prediction of equilibrium vapor pressure predictions for thin liquid films on solid surfaces. The MD simulations are particularly useful for modeling extremely thin films where the thickness of the bulk liquid region is of the same order of magnitude or smaller than that for the layered wall-affected region and the interfacial region. In such cases, the MD simulations directly account for the effects of layering and the density variation in the interfacial region.

The use of conventional disjoining pressure theory is suspect in such cases because it is generally constructed using relations derived for equilibrium of coexisting bulk phases. The conventional theory thus does not account for potential effects of direct interaction of a layered region with the interfacial region in ultra thin films. Despite the expected limitations of the conventional theory, its predictions of equilibrium vapor pressure were found to agree well with the MD simulation predictions, even for extremely thin film thicknesses where no bulk liquid region separates the wall-affected region from the interfacial region.

The model analysis developed here to explore the effects of liquid layering at the solid-liquid interface predicts that layering tends to slightly reduce the vapor pressure below that predicted by the conventional disjoining theory for a specified film thickness. The modified theory was found to not agree as well as the conventional theory with vapor pressure predictions of our MD simulations for the same film thickness. Because this modified theory adopts an extreme treatment of the near-wall layered region as a solid phase, it is expected to provide an upper bound for the effect of layering on the equilibrium vapor pressure. Even for this extreme model, the effect on vapor pressure is small, suggesting that for a real system, in which the wall region molecules have some mobility, the effects of the wall layer would be even less. Overall, the results imply that liquid layering has little, if any, effect on the equilibrium vapor pressure.

Accurate prediction of the effects of intermolecular attractive forces and associated disjoining pressure effects on equilibrium saturation properties is an important element of the analysis of transport for thin liquid films on the passage walls in micro evaporators, micro condensers, and micro heat pipes. Because of the linkage between vapor pressure and saturation temperature, the variation of vapor pressure with liquid film thickness strongly impacts the effectiveness of transport during vaporization or condensation at the interface of thin liquid films in micropassages.

Although conventional disjoining pressure theory is based on a simplistic treatment that ignores the presence of the wall-affected region and the interfacial region in the film, the results of our MD simulations and analysis indicate that, for extremely thin liquid films, conventional disjoining pressure theory nevertheless provides a prediction of the variation of vapor pressure with film thickness that is consistent with MD simulation predictions. These results enhance the credibility of models of transport in micro evaporators and micro condensers that make use of conventional disjoining pressure theory to predict local saturation conditions.

Acknowledgment

Support for this research under NSF Grant No. CTS-0456982 is gratefully acknowledged. MD simulations were performed using the Millennium workstation cluster at UC Berkeley.

Nomenclature

A_{ll} = liquid-liquid Hamaker constant
A_{ls} = liquid-solid Hamaker constant
c_i = speed of molecule i
$C_{\phi,ff}$ = fluid-fluid attractive force potential coefficient
$C_{\phi,sf}$ = solid-fluid attractive force potential coefficient
D_f = fluid molecule effective diameter
D_m = mean effective molecular diameter
D_s = solid molecule effective diameter
$\boldsymbol{F}$ = molecular force vector
$\hat{g}_l$ = molar specific Gibbs function of liquid
J = vapor boundary molecular flux
k_B = Boltzmann constant
m = molecular mass
N = number of molecules in system
N_A = Avogadro's number
P = pressure
P_d = disjoining pressure
P_l = liquid pressure
P_{ve} = vapor pressure
P_{sat} = saturation pressure for bulk equilibrium
$\bar{R}$ = universal gas constant
$\hat{s}$ = molar entropy
T = temperature
T_c = critical temperature
T_r = reduced temperature$=T/T_c$
δ_f = liquid film thickness
δ_w = wall-affected region thickness
$\hat{v}_l$ = liquid molar specific volume
v_z = z-direction molecular velocity component
Φ_{fmf} = potential energy for one fluid molecule interacting with all wall molecules
ϕ_{ff} = fluid-fluid intermolecular potential
ϕ_{LJ} = Lennard-Jones 6-12 intermolecular potential
ϕ_{sf} = solid-fluid intermolecular potential
$\hat{\rho}$ = molar density
ρ_f = Fluid molecular number density
$\rho_{l,\infty}$ = molecular number density of bulk saturated liquid
$\rho_{v,\infty}$ = molecular number density of bulk saturated vapor
ρ_s = solid wall molecular number density
$\sigma_{LJ}, \varepsilon_{LJ}$ = Lennard-Jones 6-12 potential length and energy parameters
$\hat{\mu}_l$ = liquid molar chemical potential
$\hat{\mu}_{l,sat}$ = molar chemical potential of bulk liquid at saturation
$\hat{\mu}_v$ = vapor molar chemical potential
$\hat{\mu}_{v,sat}$ = molar chemical potential of bulk vapor at saturation

References

[1] Israelachvili, J., 1992, *Intermolecular & Surface Forces*, 2nd ed., Academic, London.
[2] Kandlikar, S. G., 2002, "Fundamental Issues Related to Flow Boiling in Minichannels and Microchannels," Exp. Therm. Fluid Sci., **26**, pp. 389–407.
[3] Peterson, G. P., Duncan, A. B., and Weichold, M. H., 1993, "Experimental Investigation of Micro Heat Pipes Fabricated in Silicone Wafers," ASME J. Heat Transfer, **115**, pp. 751–756.
[4] Gerner, F. M., Badran, B., Henderson, H. T., and Ramadas, P., 1994, "Silicon-Water Micro Heat Pipes," Photochemistry, **2**, pp. 90–97.
[5] Pettersen, J., 2004, "Flow Vaporization of CO_2 in Microchannel Tubes," Exp. Therm. Fluid Sci., **28**, pp. 111–121.
[6] Park, K., and Lee, K-S., 2003, "Flow and Heat Transfer Characteristics of the Evaporating Extended Meniscus in a Micro-Capillary Channel," Int. J. Heat Mass Transfer, **46**, pp. 4587–4594.
[7] Wayner, P. C., Jr., Kao, Y. K., and LaCroix, L. V., 1976, "The Interline Heat-Transfer Coefficient of an Evaporating Wetting Film," Int. J. Heat Mass Transfer, **19**, pp. 487–492.
[8] Xu, X., and Carey, V. P., 1991, "Film Evaporation From a Micro-Grooved

Surface — An Approximate Heat Transfer Model and Its Comparison With Experimental Data," J. Thermophys. Heat Transfer, **4**, pp. 512–520.

[9] Stephan, P., and Busse, C. A., 1992, "Analysis of the Heat Transfer Coefficient of Grooved Heat Pipe Evaporator Walls," Int. J. Heat Mass Transfer, **35**, pp. 383–391.

[10] Swanson, L., and Herdt, G. C., 1992, "Model of the Evaporating Meniscus in a Capillary Tube," ASME J. Heat Transfer, **114**, pp. 434–441.

[11] Swanson, L., and Peterson, G. P., 1994, "The Evaporating Extended Meniscus in a V-Shaped Channel," J. Thermophys. Heat Transfer, **8**, pp. 172–181.

[12] Hallinan, K. P., Chebaro, H. C., Kim, S. J., and Change, W. S., 1994, "Evaporation From an Extended Meniscus for Nonisothermal Interfacial Conditions," J. Thermophys. Heat Transfer, **8**, pp. 709–716.

[13] Khrustalev, D., and Faghri, A., 1995, "Heat Transfer During Evaporation on Capillary Grooved Structures of Heat Pipes," ASME J. Heat Transfer, **117**, pp. 740–747.

[14] Wemhoff, A. P., and Carey, V. P., 2004, "Exploration of Nanoscale Features of Thin Liquid Films on Solid Surfaces Using Molecular Dynamics Simulations," Paper No. IMECE2004-59429, *Proceedings of the 2004 ASME International Mechanical Engineering Conference and RD&D Exposition*.

[15] Box, G. E. P., and Mueller, M. E., 1958, "A Note on the Generation of Random Normal Deviates," Ann. Math. Stat., **29**, pp. 610–611.

[16] Toxvaerd, S., 1981, "The Structure and Thermodynamics of a Solid-Fluid Interface," J. Chem. Phys., **74**, pp. 1998–2005.

[17] Rowley, L. A., Nicholson, D., and Parsonage, N. G., 1976, "Grand Ensemble Monte Carlo Studies of Physical Adsorption. I. Results for Multilayer Adsorption of 12-6 Argon in the Field of a Plane Homogeneous Solid," Mol. Phys., **31**, pp. 365–387.

[18] Wendland, M., Salzmann, S., Heinbuch, U., and Fischer, J., 1989, "Born-Green-Yvon Results for Adsorption of a Simple Fluid on Plane Walls," Mol. Phys., **67**, pp. 161–172.

[19] Carey, V. P., 1999, *Statistical Thermodynamics and Microscale Thermophysics*, Cambridge U. P., Cambridge.

[20] Andersen, H. C., 1980, "Molecular Dynamics at Constant Pressure and/or Temperature," J. Chem. Phys., **72**, pp. 2384–2393.

[21] Frenkel, D., and Smit, B., 2002, *Understanding Molecular Simulation; From Algorithms to Applications*, 2nd ed., Academic, San Diego.

[22] Carey, V. P., and Hawks, N. E., 1995, "Stochastic Modeling of Molecular Transport to an Evaporating Microdroplet in a Superheated Gas," ASME J. Heat Transfer, **117**, pp. 432–439.

[23] Allen, M. P., and Tildesley, D. J., 1987, *Computer Simulation of Liquids*, Clarendon, Oxford.

[24] Liu, K. S., 1974, "Phase Separation of Lennard-Jones Systems: A Film in Equilibrium with Vapor," J. Chem. Phys., **60**, pp. 4226–4230.

[25] Wendland, M., Heinbuch, U., and Fischer, J., 1989, "Adsorption of Simple Gas Mixtures on a Plane Wall: Born-Green-Yvon Results for Structure, Adsorption Isotherms and Selectivity," Fluid Phase Equilib., **48**, pp. 259–277.

[26] American Society of Heating, Refrigerating, and Air-conditioning Engineers, 2001, *ASHRAE Fundamentals Handbook*, ASHRAE, Atlanta.

[27] Dunikov, D. O., Malyshenko, S. P., and Zhakhovskii, V. V., 2001, "Corresponding States Law and Molecular Dynamics Simulations of the Lennard-Jones Fluid," J. Chem. Phys., **115**, pp. 6623–6631.

[28] Lotfi, A., Vrabec, J., and Fischer, J., 1992, "Vapour Liquid Equilibria of the Lennard-Jones Fluid from the NPT Plus Test Particle Method," Mol. Phys., **76**, pp. 1319–1333.

[29] Weng, J. G., Park, S., Lukes, J. R., and Tien, C. L., 2000, "Molecular Dynamics Investigation of Thickness Effect on Liquid Films," J. Chem. Phys., **113**, pp. 5917–5923.

[30] Carey, V. P., 1992, *Liquid-Vapor Phase Change Phenomena*, Taylor and Francis, New York.

[31] Xue, L., Keblinski, P., Phillpot, S. R., Choi, S. U.-S., and Eastman, J. A., 2004, "Effect of Liquid Layering at the Liquid-Solid Interface on Thermal Transport," Int. J. Heat Mass Transfer, **47**, pp. 4277–4284.